Monthly Notices of the ROYAL ASTRONOMICAL SOCIETY

MNRAS **518,** 5313–5322 (2023) https://doi.org/10.1093/mnras/stac3128
Advance Access publication 2022 November 4

r-process nucleosynthesis and kilonovae from hypermassive neutron star post-merger remnants

Sanjana Curtis [1]★ Philipp Mösta,[2]★ Zhenyu Wu [3] David Radice [4,5,6] Luke Roberts,[7] Giacomo Ricigliano [8] and Albino Perego[8,9]

[1]*Anton Pannekoek Institute for Astronomy, University of Amsterdam, Science Park 904, Amsterdam 1098 XH, The Netherlands*
[2]*GRAPPA, Anton Pannekoek Institute for Astronomy and Institute of High-Energy Physics, University of Amsterdam, Science Park 904, Amsterdam 1098 XH, The Netherlands*
[3]*School of Astronomy and Space Science, Nanjing University, Nanjing 210023, China*
[4]*Institute for Gravitation and the Cosmos, The Pennsylvania State University, University Park, PA 16802, USA*
[5]*Department of Physics, The Pennsylvania State University, University Park, PA 16802, USA*
[6]*Department of Astronomy & Astrophysics, The Pennsyvlania State University, University Park, PA 16802, USA*
[7]*Computer, Computational, and Statistical Sciences Division, Los Alamos National Laboratory, Los Alamos, NM 87545, USA*
[8]*Dipartimento di Fisica, Università di Trento, Via Sommarive 14, Trento 38123, Italy*
[9]*INFN-TIFPA, Trento Institute for Fundamental Physics and Applications, ViaSommarive 14, Trento I-38123, Italy*

Accepted 2022 October 27. Received 2022 October 27; in original form 2021 December 14

ABSTRACT

We investigate *r*-process nucleosynthesis and kilonova emission resulting from binary neutron star (BNS) mergers based on a three-dimensional (3D) general-relativistic magnetohydrodynamic (GRMHD) simulation of a hypermassive neutron star (HMNS) remnant. The simulation includes a microphysical finite-temperature equation of state (EOS) and neutrino emission and absorption effects via a leakage scheme. We track the thermodynamic properties of the ejecta using Lagrangian tracer particles and determine its composition using the nuclear reaction network `SkyNet`. We investigate the impact of neutrinos on the nucleosynthetic yields by varying the neutrino luminosities during post-processing. The ejecta show a broad distribution with respect to their electron fraction Y_e, peaking between ∼0.25–0.4 depending on the neutrino luminosity employed. We find that the resulting *r*-process abundance patterns differ from solar, with no significant production of material beyond the second *r*-process peak when using luminosities recorded by the tracer particles. We also map the HMNS outflows to the radiation hydrodynamics code `SNEC` and predict the evolution of the bolometric luminosity as well as broadband light curves of the kilonova. The bolometric light curve peaks on the timescale of a day and the brightest emission is seen in the infrared bands. This is the first direct calculation of the *r*-process yields and kilonova signal expected from HMNS winds based on 3D GRMHD simulations. For longer-lived remnants, these winds may be the dominant ejecta component producing the kilonova emission.

Key words: neutron star mergers – magnetohydrodynamics – nuclear reactions, nucleosynthesis, abundances.

1 INTRODUCTION

The inspiral and merger of binary neutron stars is accompanied by the ejection of neutron-rich matter that undergoes rapid neutron capture (*r*-process) nucleosynthesis (Lattimer et al. 1977; Symbalisty & Schramm 1982; Meyer 1989; Goriely, Bauswein & Janka 2011; Cowan et al. 2021). Radioactive decay of unstable *r*-process nuclei synthesized in these ejecta can power an electromagnetic transient called a kilonova (Li & Paczyński 1998; Metzger et al. 2010; Roberts et al. 2011; Kasen, Badnell & Barnes 2013). In August 2017, gravitational waves from the merger of a pair of neutron stars were detected for the first time along with their kilonova counterpart: GW170817 (Abbott et al. 2017) and AT2017gfo (Coulter et al. 2017; Soares-Santos et al. 2017; Arcavi et al. 2017), respectively. The electromagnetic spectrum of this kilonova provided the first direct evidence that such mergers are a site where *r*-process nucleosynthesis takes place and produces the heaviest elements in our Universe (Kasen et al. 2017; Pian et al. 2017). The observed kilonova emission started out with a featureless thermal spectrum that peaked at ultraviolet/optical frequencies (Evans et al. 2017; McCully et al. 2017; Nicholl et al. 2017), rapidly evolving over the next few days to show a spectral peak in the near-infrared (Pian et al. 2017; Tanvir et al. 2017; Chornock et al. 2017). This behaviour of the kilonova associated with GW170817 is usually interpreted as resulting from distinct ejecta components, giving rise to the early blue and late red peaks (Cowperthwaite et al. 2017; Drout et al. 2017). Relatively neutron-rich ejecta that synthesize a substantial mass fraction of lanthanides, which are opaque to blue light, produce a 'red' kilonova, whereas the 'blue' kilonova is understood as emission arising from a less neutron-rich, lanthanide-poor component of the ejecta with a correspondingly lower opacity.

The total ejecta mass inferred for the red kilonova component is $M_{\rm red} \approx 5 \times 10^{-2}\,{\rm M}_\odot$, with an electron fraction $Y_e \lesssim 0.2$ and moving

★ E-mail: sanjanacurtis@uchicago.edu (SC); p.moesta@uva.nl (PM)

at a mean velocity of $v_{\rm red} \approx 0.1c$ (Villar et al. 2017). The dynamical merger ejecta and/or outflows from the remnant accretion torus, the latter possibly being the dominant component, can provide the red kilonova ejecta. The origin of the blue kilonova is less understood. The ejecta properties derived for the blue component include a total mass $M_{\rm blue} \approx 2 \times 10^{-2}\,{\rm M}_{\odot}$, high velocities $v_{\rm blue} \approx 0.2$–$0.3c$ and a relatively high $Y_e \approx 0.25$–0.35. Shock-heated polar dynamical ejecta can produce high-velocity outflows with the requisite Y_e but cannot account for the large quantity of mass needed to explain the blue kilonova. Neutrino-driven winds from an hypermassive neutron star (HMNS) remnant offer another possible explanation since they experience enhanced neutrino reprocessing that drives up the Y_e. However, most simulations so far have found mass-averaged velocities no larger than $\sim 0.1c$ for these winds (Fahlman & Fernández 2018), much slower than inferred for the blue component. An alternative explanation was suggested by Metzger, Thompson & Quataert (2018) who proposed that neutrino-heated, magnetically-accelerated winds from a strongly magnetized HMNS remnant could simultaneously provide the high total mass, high velocity, as well as the relatively high Y_e needed to produce a blue kilonova. Another possible mechanism powering the blue kilonova was suggested in Nedora et al. (2019), who found that spiral density waves in the remnant generate a wind of mass $\sim 10^{-2}\,{\rm M}_{\odot}$, velocity $\sim 0.2c$, and typical ejecta Y_e above 0.25.

Recently, Mösta et al. (2020) have carried out high-resolution three-dimensional (3D) dynamical general-relativistic magnetohydrodynamic (GRMHD) simulations where they evolve a post-merger HMNS remnant with an initial poloidal magnetic field. They found a magnetized neutron-rich wind driven from the HMNS, which ejects material at a rate of $\sim 0.1\ {\rm M}_{\odot}\ {\rm s}^{-1}$ resulting in a total ejecta mass of $5 \times 10^{-3}\,{\rm M}_{\odot}$. These HMNS ejecta thus represent an important component of binary neutron star (BNS) ejecta in addition to the dynamical ejecta ($10^{-4}\ {\rm M}_{\odot} < M_{\rm ej} < 10^{-2}\,{\rm M}_{\odot}$) and winds driven from the accretion disk once a black hole (BH) has formed. For longer-lived remnants, they could be the dominant ejecta component. The magnetized outflows also have a broad distribution in velocity space, with a significant fraction of the material with velocities in the range of $0.3c \lesssim v^r \lesssim 0.5c$, setting these ejecta apart from the dynamical ejecta ($v^r < 0.3c$) and the accretion disk winds ($v^r < 0.1c$).

In this work, we post-process the HMNS outflow to track the *r*-process abundances in the ejecta. We calculate abundances using different constant neutrino luminosities during post-processing in addition to using luminosities recorded by the tracer particles. This allows us to constrain the impact of uncertainties introduced by the approximate neutrino leakage scheme employed in the dynamical simulation. We map the outflow to a spherically-symmetric radiation hydrodynamics code and track its further evolution to predict the bolometric light curve of the resulting kilonova. We also produce light curves in different bands under the assumption of blackbody emission. We find that these ejecta do not produce a robust *r*-process up to the third *r*-process peak. The bolometric light curve of the kilonova evolves quickly and reaches a peak luminosity of $\sim 10^{41}$ erg s^{-1} at around 1 d, with the brightest emission observed in the infrared bands.

The paper is organized as follows. In Section 2, we describe our input models, mapping procedure, and numerical codes used to compute abundances and light curves. In Section 3.1, we present the ejecta composition followed by the bolometric and broadband light curves of the kilonova in Section 3.2. We discuss the implications of our results and future directions in Section 4.

2 METHODS

2.1 Input models

We study model B15-low, presented in Mösta et al. (2020) where an HMNS post-merger remnant is evolved with an initial poloidal magnetic field of strength 10^{15} G. The simulation employs ideal GRMHD using the `Einstein Toolkit` and includes the $K_0 = 220$ MeV variant of the equation of state of Lattimer & Swesty (1991). Neutrinos are treated via an approximate leakage/heating scheme that captures the overall energetics and lepton number exchange due to neutrino emission and absorption (O'Connor & Ott 2010; Ott et al. 2013). This scheme tracks three neutrino species: electron flavor neutrinos ν_e, electron flavor antineutrinos $\bar{\nu}_e$, and all the heavy-lepton flavor neutrinos grouped together into a single species called ν_x. The scheme captures the overall neutrino energetics correctly up to a factor of a few compared to full neutrino transport in simulations of core-collapse supernovae (O'Connor & Ott 2010). It does not account for momentum deposition, energy dependence, or neutrino pair-annihilation.

The HMNS evolved using the set-up described above was formed in the merger of an equal-mass binary with individual NS masses of 1.35 ${\rm M}_{\odot}$ at infinity, originally simulated in GRHD with the `WhiskyTHC` code in Radice et al. (2018). It is mapped as initial data at 17 ms post-merger, adding a poloidal magnetic field of strength $B_0 = 10^{15}$ G. We make sure our initial data are consistent by performing a primitive to conservative variable conversion similarly to how magnetized binary neutron-star initial data is constructed. In the early post-mapping evolution, the magnetic field adjusts rapidly to the underlying fluid configuration as a result of the ideal magnetohydrodynamics (MHD) assumption but this transient lasts only the first 2 ms. The detailed mapping procedure is outlined in Mösta et al. (2020).

During the course of the simulation, this initial magnetic field is amplified due to magnetic resonance imaging-induced turbulence in the HMNS to magnetar strengths. A magnetized neutron-rich wind is driven from the HMNS, which ejects material at a rate of $\sim 4.6 \times 10^{-2}\,{\rm M}_{\odot}\ {\rm s}^{-1}$ and accounts for the majority of the ejected mass. Magnetic fields collimate part of the outflow into a mildly relativistic jet. The total ejecta mass estimated from the low-resolution simulation is $1.1 \times 10^{-3}\,{\rm M}_{\odot}$, making these ejecta an important component in BNS mergers for both *r*-process nucleosynthesis and the resulting kilonova. The outflow persists until the HMNS collapses to a black hole ~21 ms after the start of the simulation i.e. ~38 ms post-merger.

In Fig. 1 we present histograms of the radial velocity of the unbound material (top four panels) and its Y_e (bottom four panels) at different times during the evolution of the system. The unbound material is determined via the Bernoulli criterion $-hu_t > 1$, where h is the relativistic enthalpy of the magnetized fluid. The ejecta show a broad distribution in velocity space. At all times, there exists a significant amount of material with velocities between $0.3c < v^r < 0.4c$. As the system evolves, velocities $0.4\ c < v^r < 0.48\ c$ are also seen for a small fraction of the ejecta. The Y_e is a measure of the neutron-richness of matter, given by:

$$Y_e \equiv \frac{n_p}{n_n + n_p} \tag{1}$$

where n_n and n_p are the densities of neutrons and protons respectively. In the ejecta, neutrino-matter interactions drive the Y_e towards higher values i.e. towards less neutron-rich conditions. Most of the ejected material has Y_e values between 0.2 and 0.3, with a peak around $Y_e \sim 0.25$. This has interesting implications for *r*-process yields since

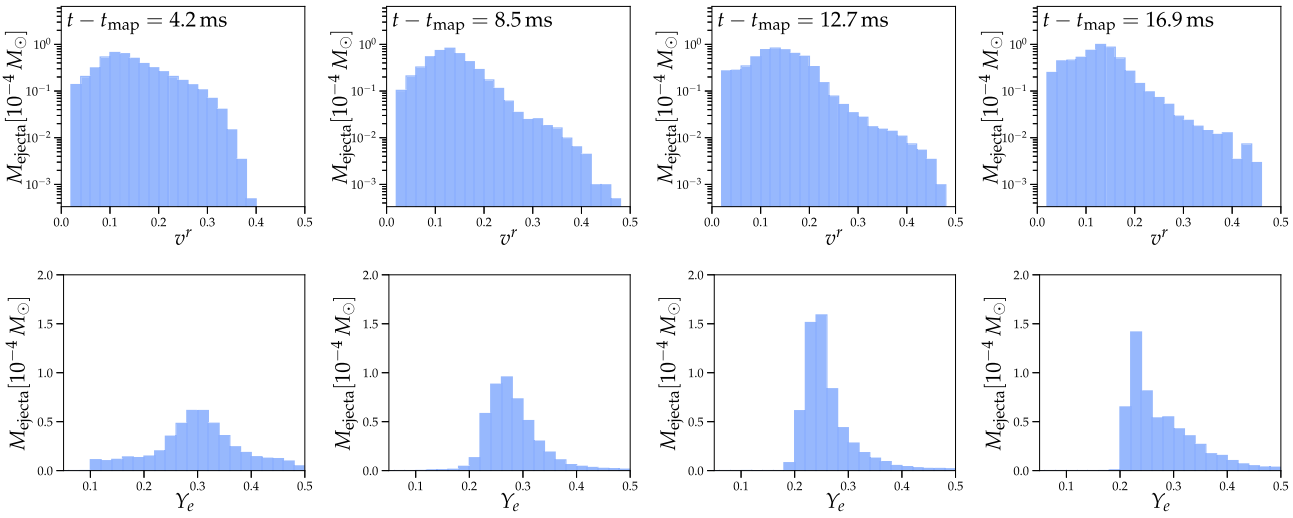

Figure 1. Histograms of the radial velocity v^r of the unbound material (top panels), where r is the radius in spherical coordinates, and the Y_e of the unbound material (bottom panels) at different times during the dynamical simulation. Each column corresponds to a different time in the evolution of the system.

Y_e values above ~ 0.25 can inhibit the synthesis of any significant amount of heavy elements and the resulting abundance pattern is quite sensitive to the ejecta properties.

2.2 Tracer particles and nucleosynthesis

We extract the thermodynamic conditions of the ejected material and the neutrino luminosities it has encountered from the hydrodynamical simulation using Lagrangian tracer particles. The tracers are uniformly spaced to represent regions of constant volume. At the start of the simulation, each tracer particle is assigned a mass that accounts for the density at its location and the volume the particle covers. We place 96 000 tracer particles to ensure that a sufficient number of tracer particles are present in the outflow. The particles are advected passively with the fluid and data from the 3D simulation grid are interpolated to the tracer position and recorded as a function of time. The tracers are collected at a surface defined by a chosen radius, $r = 150\ {\rm M}_\odot = 222$ km here, and tracer quantities are frozen once the tracer particle crosses this surface.

We track the ejecta composition by post-processing the tracer particles with the open-source nuclear reaction network `SkyNet` (Lippuner & Roberts 2017). The network includes 7852 isotopes up to ^{337}Cn. Forward strong rates are taken from REACLIB (Cyburt et al. 2010) and inverse rates are obtained using detailed balance. The weak rates employed here come from Fuller, Fowler & Newman (1982), Oda et al. (1994), Langanke & Martínez-Pinedo (2000), or from REACLIB. The nuclear masses and partition functions are also obtained from REACLIB. Rates for neutron-induced fission reactions with symmetric fission fragments are take from Panov, Ptitsyn & Chechetkin (1995) and spontaneous fission rates are calculated from the approximation of Frankel & Metropolis (1947) using the spontaneous fission barriers of Mamdouh et al. (2001). Rates of neutrino emission and absorption reactions on free neutrons and protons are calculated as described in Lippuner & Roberts (2017).

The network is started in nuclear statistical equilibrium (NSE) when the particle temperature drops below 20GK. The network evolves the temperature by calculating source terms due to individual nuclear reactions and neutrino interactions. The neutrino luminosities recorded by the tracers are noisy due to interpolation effects and high time resolution. We perform a moving-window time average of the luminosity data of the form $\nu_{{\rm av},i} = \alpha \cdot \bar{\nu}_i + (1-\alpha) \cdot \nu_{{\rm av},i-1}$, where i denotes the current and $i-1$ the previous timestep. The weight function for each data set in the moving average is chosen as $\alpha = 2(n+1)^{-1}$, with $n = 19$. We keep the luminosities constant after the end of the tracer data.

The dynamical simulation implements a leakage scheme that aims to capture the overall energetics and lepton number exchange due to neutrino emission and absorption. Realistic neutrino luminosities may differ by up to a factor of a few from those extracted by the tracer particles (O'Connor & Ott 2010). Since the detailed ejecta composition does depend sensitively on the accuracy of the neutrino transport, the uncertainty in our leakage scheme will translate into uncertainties in the r-process abundances predicted here. `SkyNet` allows us to set the neutrino luminosities and energies to constant values during post-processing. We take advantage of this capability to explore the impact of varying the neutrino luminosity over a chosen range i.e. assuming constant values of zero (neglecting neutrinos), 10^{51}, 10^{52}, and 10^{53} erg s^{-1} (artificially high). The luminosities are set to be the same for electron neutrinos as well as antineutrinos while the average neutrino energies are chosen as 12 and 14 MeV, respectively. We compare the resulting abundances to those obtained for the case where we use neutrino luminosities recorded by the tracer particles. The tracer neutrino luminosities are typically a few 10^{52} erg s^{-1} and thus fall between the constant luminosity cases of 10^{52} and 10^{53} erg s^{-1}. In this way, we constrain the impact of uncertainties in neutrino luminosities on the final abundances.

The dynamical simulation, and hence the tracer trajectory, ends within few milliseconds due to the high computational expense of the simulation. However, the requisite conditions for nucleosynthesis usually still exist at this point. The network continues the calculation up to a desired end time by smoothly extrapolating the particle data beyond the end of the trajectory under the assumption of homologous expansion. The network expands the particle using $\rho \propto t^{-3}$ until a minimum temperature is reached. Our calculations are carried out to 10^9s, which is sufficient to generate a stable abundance pattern as a function of mass number. The evolution of the tracer temperature and density

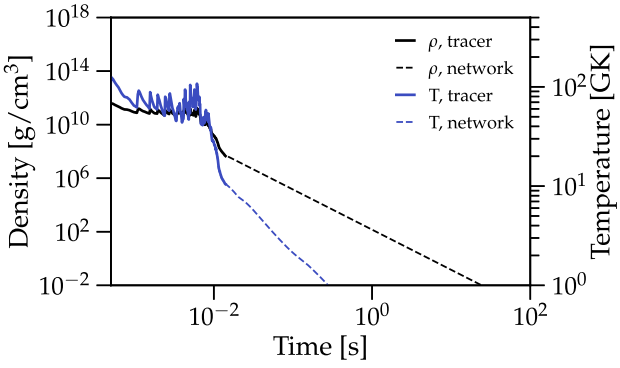

Figure 2. The evolution of density (black lines) and temperature (blue lines) for a representative tracer particle. The solid lines show the original tracer particle data while the dashed lines show the data extrapolated by SkyNet under the assumption of homologous expansion. This evolution corresponds to the case where zero neutrino luminosity is employed during post-processing.

within SkyNet is shown for a representative tracer particle in Fig. 2.

2.3 Radiation transport and mapping

SNEC (Morozova et al. 2015; Wu et al. 2021) is a one-dimensional Lagrangian equilibrium-diffusion radiation hydrodynamics code capable of simulating the hydrodynamical evolution of merger ejecta and the resulting kilonova emission. For kilonova modeling, the nickel heating term relevant for the supernova case in SNEC is replaced by a prescription for radioactive heating due to decay of *r*-process nuclei. The time-dependent heating rate is derived in Wu et al. (2021) based on the nucleosynthesis calculations of Perego et al. (2020) by constructing fits over a comprehensive grid of 11700 trajectories, covering a wide range of Y_e, entropy s and expansion timescale τ: $0.01 \leq Y_e \leq 0.48$, $1.5\ k_B$ baryon$^{-1} \leq s \leq 200\ k_B$ baryon^{-1} and $0.5\ \text{ms} \leq \tau \leq 200\ \text{ms}$. At early times $t \lesssim 0.1$ d, fits are constructed using the analytic formula proposed by Korobkin et al. (2012). At later times $t \gtrsim 0.1$ d, a power-law fit is used. The two regimes are joined together via a smoothing procedure and the overall fit describes the heating rate over a time interval ranging from 0.1 s to 50 d post-merger. We additionally assume a constant thermalization efficiency of 0.5 taking into account energy loss by neutrinos and partial thermalization of photons, fast electrons, and excited nuclei in the expanding ejecta.

To describe the non-trivial photon–matter interactions, we use an effective wavelength-independent (or grey) opacity κ to fit the values in Tanaka et al. (2018) computed from detailed energy dependent, radiative transfer simulations. In particular, κ is set as a function of the initial Y_e (i.e. before nucleosynthesis) of the ejecta as:

$$\kappa = 1 + \frac{9}{1 + (4Y_e)^{12}}\ \text{cm}^2\ \text{g}^{-1}. \tag{2}$$

The minimum opacity is 1 cm^2 g^{-1} and the maximum is 10 cm^2 g^{-1}. The exponent of 12 makes the opacity drop steeply near $Y_e = 0.25$. This spans the overall range of opacities found for low, intermediate and high Y_e material in keeping with the resulting abundances of heavy lanthanides in the ejecta. The steep transition around $Y_e = 0.25$ accounts for the steep decrease in typical lanthanide mass fractions from > 0.1 to 10^{-4} that occurs over an extremely narrow range in Y_e centered at $Y_e \approx 0.25$.

We do not use the detailed ejecta composition for the kilonova calculation. A simplified version of the Paczynski equation of state is employed where the Saha equations are not solved and the correction terms for partial ionization are ignored. We use a value of 2.0 to specify the mean degree of ionization. It is possible to inject additional energy into the ejecta via a thermal bomb but we do not require this capability and therefore set the thermal bomb energy to zero.

SNEC computes the evolution of the bolometric luminosity as well as AB magnitudes in different bands assuming blackbody radiation. The bolometric luminosity is computed as the sum of the luminosity at the photosphere and the radioactive heating above the photosphere. The location of the photosphere is defined by the optical depth $\tau = 2/3$ and the luminosity at the photosphere is given by the usual expression for radiative luminosity calculated at its location:

$$L = -(4\pi r^2)^2 \frac{\lambda a c}{3\kappa} \frac{\partial T^4}{\partial m} \tag{3}$$

where r is the radius, λ is the flux-limiter, a is the radiation constant, and m is the mass coordinate. The effective temperature at the photosphere is calculated from the bolometric luminosity L at the photosphere and the photospheric radius R_{ph} as $T_{\text{eff}} = (L/4\pi\sigma R_{\text{ph}}^2)^{1/4}$, where σ is the Stefan-Boltzmann constant. To compute the AB magnitudes in different observed wavelength bands, SNEC assumes blackbody radiation at the effective temperature computed at the photosphere and for the layers above the photosphere. While non-thermal radiation is negligible at $T \sim 5000\ K$ (Kasen et al. 2013), it becomes important at late times as the ejecta become transparent. It should be noted that the late time light curves are unreliable since the blackbody approach fails as the ejecta become optically thin.

As input, SNEC requires the radius, temperature, density, velocity, initial Y_e, initial entropy, and expansion timescale of the outflow as a function of mass coordinate. The entropy s and expansion timescale τ are used to compute the heating rates and opacities as discussed above. The outflow properties are recorded by measuring the flux of the relevant quantities through a spherical surface at radius $r = 100\ \text{M}_\odot = 148$ km. The unbound material is determined from these two-dimensional data using the Bernoulli criterion and the mass-weighted angle-averaged outflow profile is computed as a function of the enclosed ejecta mass m. Since the initial data for SNEC are required at a fixed time, the data are transformed assuming homologous expansion and the radius $r(m)$ is computed from the requirement that $m(r) = 4\pi \int_0^r \rho r^2 dr$.

3 RESULTS

3.1 *r*-process nucleosynthesis

The Y_e of the ejecta is one of the most critical quantities for determining its ultimate composition. For typical entropy and expansion timescales occurring in the ejecta from BNS mergers, a strong *r*-process occurs for $Y_e \lesssim 0.2$. The resulting abundance pattern is usually robust and relatively insensitive to the exact Y_e, especially for low enough Y_e, due to the occurrence of fission cycling. Ejecta with $0.25 \lesssim Y_e \lesssim 0.4$, on the contrary, will not produce substantial abundances of the heavy lanthanides with $A \gtrsim 140$ and the composition is a lot more sensitive to the outflow properties. For $Y_e \gtrsim 0.4$–0.5, only a weak *r*-process or a composition dominated exclusively by Fe-group nuclei may be obtained.

The electron-flavor neutrinos and anti-neutrinos play a crucial role in setting the relative ratio of neutrons to protons and hence the Y_e

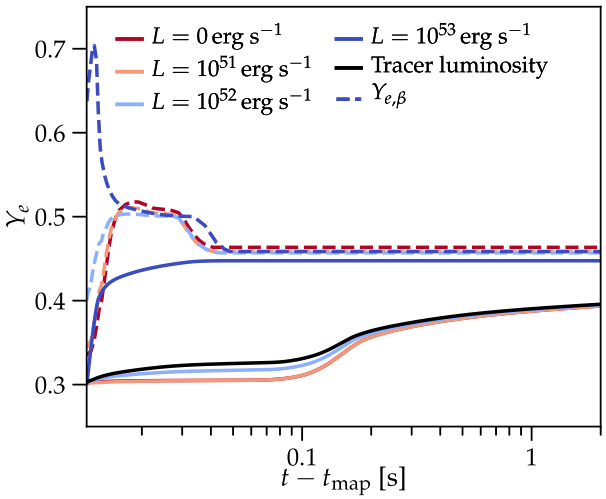

Figure 3. The figure shows the Y_e as a function of time for a representative particle. Different colored lines indicate results for different constant neutrino luminosities used in the SkyNet calculation and the black line indicates results obtained using the neutrino luminosities recorded by the tracer particles. The dashed lines indicate the evolution of $Y_{e,\beta}$ for the different luminosity settings.

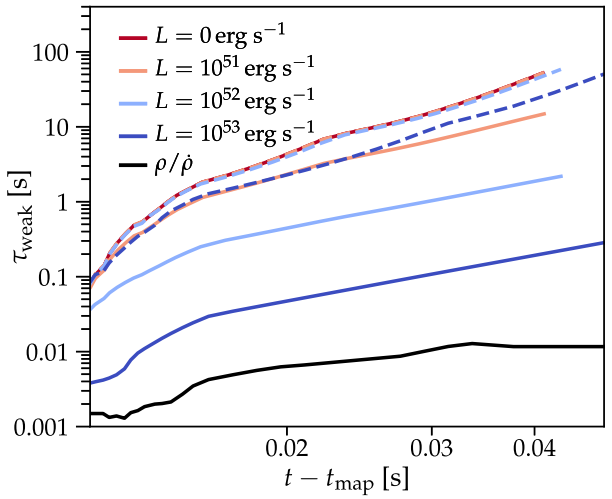

Figure 4. The figure shows the weak interaction and dynamical timescales for a representative particle. Different colored lines indicate weak interaction timescales for different constant neutrino luminosities used in the SkyNet calculation while the black line shows the corresponding dynamical timescale. The dashed lines indicate the lepton capture timescale $(\lambda_{e^-} + \lambda_{e^+})^{-1}$.

through the charged-current reactions on free nucleons:

$$\nu_e + n \rightleftharpoons p + e^-$$
$$\bar{\nu}_e + p \rightleftharpoons n + e^+. \tag{4}$$

Weak interactions will drive the Y_e in the neutron-rich wind towards its equilibrium value $Y_{e,\beta}$, given by (Qian & Woosley 1996):

$$Y_{e,\beta} \simeq \left(1 + \frac{L_{\bar{\nu}_e}}{L_{\nu_e}} \frac{\epsilon_{\bar{\nu}_e} - 2\Delta + 1.2\Delta^2/\epsilon_{\bar{\nu}_e}}{\epsilon_{\nu_e} + 2\Delta + 1.2\Delta^2/\epsilon_{\nu_e}}\right)^{-1} \approx 0.4 - 0.6, \tag{5}$$

where $\Delta \equiv (m_n - m_p)c^2$ is the neutron–proton mass difference and $\epsilon_\nu = \langle E_\nu^2\rangle/\langle E_\nu\rangle$, where $\langle E_\nu^n\rangle$ denotes the nth neutrino energy moment of the neutrino energy distribution. The range of $Y_{e,\beta}$ comes from the difference between the spectra of electron flavor neutrinos and antineutrinos coming from the HMNS and thus depends on the detailed neutrino transport. Both the neutrino fluxes and the thermodynamic state, e.g. density, of the material also determine the lepton capture rates. As the magnetic field accelerates matter away from the remnant, electron neutrinos will convert the initially neutron-rich composition back towards $Y_e = Y_{e,\beta}$. The final Y_e in the outflow depends on the weak interaction timescale relative to the dynamical timescale but is always driven towards the equilibrium value. Weak interactions push Y_e towards $Y_{e,\beta}$ on a timescale given by $\tau_{weak} = (\lambda_{e^-}(\rho, T, Y_e) + \lambda_{e^+}(\rho, T, Y_e) + \lambda_{\nu_e} + \lambda_{\bar{\nu}_e})^{-1}$. If τ_{weak} is shorter than the dynamical timescale, $\tau_d = \rho/\dot{\rho}$, the material should attain a composition determined by $Y_{e,\beta}$. In Fig. 3, we present the Y_e as a function of time for a representative tracer particle. The corresponding dynamical and weak interaction timescales are shown in Fig. 4. The evolution of these quantities is shown for calculations using different constant luminosities during post-processing in addition to the case where luminosities recorded by the tracer particle are employed. For the constant luminosity calculations, we assume $L_{\nu_e} = L_{\bar{\nu}_e}$ and constant mean neutrino energies $\langle\epsilon_{\nu_e}\rangle = 10$ MeV and $\langle\epsilon_{\bar{\nu}_e}\rangle = 14$ MeV. For this particle, and as is typical for this outflow, the dynamical timescale remains smaller than the weak interaction timescale for all luminosity settings and thus while the Y_e is always moving towards its weak equilibrium value, weak equilibrium is never obtained.

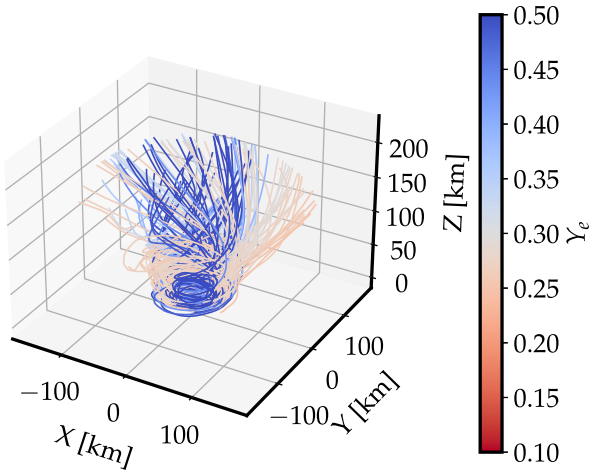

Figure 5. 3D spatial trajectories of all tracer particles constituting the HMNS ejecta. The tracers are colour coded to represent the Y_e value attained at the end of the dynamical simulation.

In general, high neutrino luminosities in the polar region lead to an increase in the Y_e in this region and the longer a particle dwells here, the higher is its final Y_e. In Fig. 5, we show the paths of all our tracer particles colour-coded by their 'final' Y_e (right) at the end of the tracer data. As is evident from the Figure, material that is closer to the polar axis has higher Y_e values at the end of the dynamical simulation. This trend in Y_e is preserved during further evolution within SkyNet as the temperature drops below 5 GK and r −process nucleosynthesis begins.

In Fig. 6, we show the distribution of the Y_e for all ejected tracers when the temperature of the particles is last above 5 GK, as computed within SkyNet. Since 5 GK is the temperature around which r-process nucleosynthesis starts, the Y_e value at this point is the relevant quantity for setting r-process yields. We show these quantities for the calculation that uses the leakage neutrino luminosities recorded by the tracer particles, typically of the order of a few times 10^{52}erg s^{-1}, as well as for calculations carried out assuming different constant values

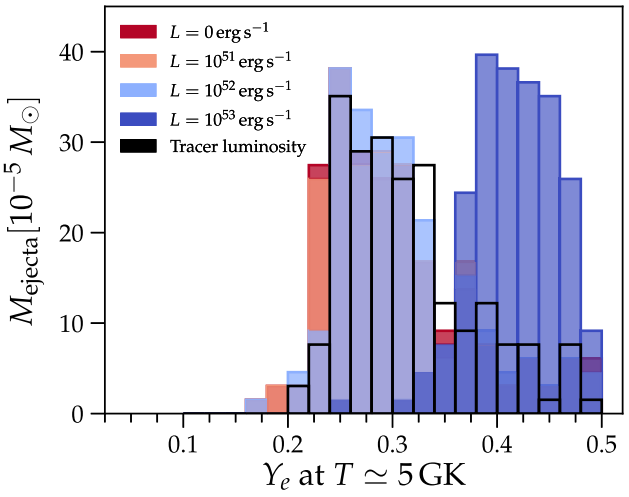

Figure 6. Ejecta Y_e histograms when the particles are last above a temperature of 5 GK. The different colors correspond to results obtained with different constant neutrino luminosities used in the network calculations. The black, unfilled histogram shows results obtained using the neutrino luminosities recorded by the tracer particles.

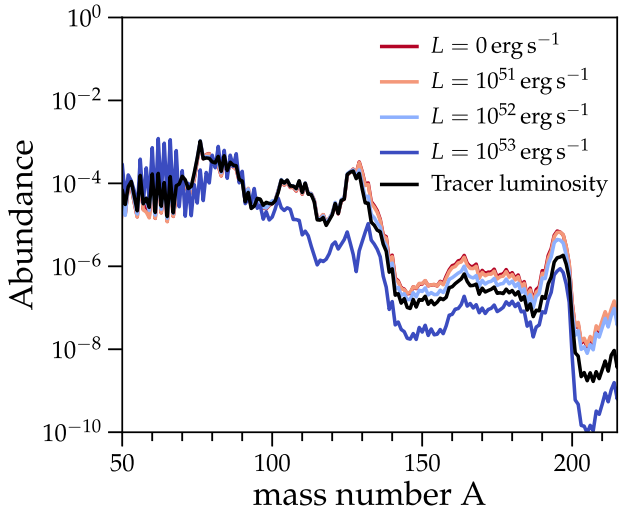

Figure 7. Fractional abundances as a function of mass number A for HMNS ejecta. Different colored lines correspond to results obtained with different neutrino luminosities in the nuclear reaction network calculation.

of the neutrino luminosities. Higher constant neutrino luminosities noticeably shift the peak of the Y_e distribution towards higher values. In the extreme case of $L_\nu = 10^{53}$ erg s^{-1}, the ejecta Y_e peaks around ∼0.4, above which the synthesis of both the second and third *r*-process peaks is suppressed and only a weak *r*-process can occur.

These variations seen in the Y_e distributions for the different neutrino luminosity scenarios are reflected in the resulting abundance patterns. In Fig. 7, we plot the final abundances averaged over all tracers as a function of mass number and compare the results obtained for the four constant luminosity cases and those obtained using the luminosity recorded by the tracer particles. In all cases, there is some production of elements up to the third *r*-process peak but we do not see a robust *r*-process for any of the scenarios. The abundances obtained for the zero luminosity case and the 10^{51} erg s^{-1} constant luminosity case are almost identical. Starting with luminosities of 10^{52} erg s^{-1}, we find that the production of heavy nuclei with $A \gtrsim$ 140 is further suppressed. The reduction in the abundances beyond A ∼ 140 is accompanied by larger production of nuclei with 50 ≤ A ≤ 80. However, these three cases still show a significant production of nuclei of the second *r*-process peak. For a constant luminosity of 10^{53} erg s^{-1}, the production of the second peak is also suppressed and the abundances of the heavy *r*-process elements are reduced by up to a factor of ∼10 compared to the zero luminosity case. This is consistent with the expected outcome for an electron-fraction distribution that is peaked around ∼0.4 given the dynamical timescales and entropies explored here.

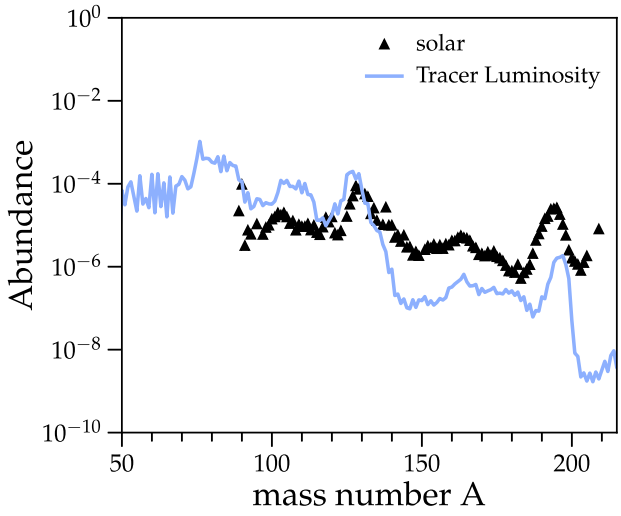

Figure 8. Fractional abundance pattern as a function of mass number A for the HMNS ejecta using neutrino luminosities recorded by the tracer particles during post-processing. Black triangles show the solar abundance pattern scaled to match the second r-process peak at $A = 135$.

Finally, in Fig. 8 we present the fractional abundance pattern as a function of mass number obtained for the HMNS ejecta using the tracer luminosities, compared directly to solar abundances. The solar abundance pattern has been scaled to match the second *r*-process peak at $A \sim 135$. We find that the abundances beyond A ∼ 140 including the third *r*-process peak are underproduced by up to an order of magnitude or more while lighter nuclei with A ≲ 135 are overproduced in these ejecta.

3.2 Kilonova

The unstable *r*-process nuclei synthesized in the merger ejecta undergo radioactive decay, heating the ejecta and powering an electromagnetic transient known as a kilonova. The mass and velocity of the ejecta, the radioactive heating rate, the thermalization efficiency of decay products, and the ejecta opacity all play a key role in determining the luminosity evolution of this transient. The opacity in particular sets the time and wavelength(s) at which the ejecta become transparent and in turn depends on the composition of the ejected material.

In Fig. 9, we present the averaged velocity, temperature, electron fraction, and opacity profiles of the HMNS outflow used as input for SNEC. The total ejecta mass is $\sim 7.5 \times 10^{-3}\,\mathrm{M}_\odot$, most of it extremely hot with temperatures between ∼ 9 and 16 GK and moving at velocities between ∼ 0.15 and 0.2c. In Fig. 10, we show 3D volume renderings of the Bernoulli criterion for the outflow, along with an isocontour plot for a density of 10^{10} g cm^{-3}. The narrow red funnel aligned with rotation axis (z-axis) shows the mildly relativistic jet while blue corresponds to material with lower Lorentz

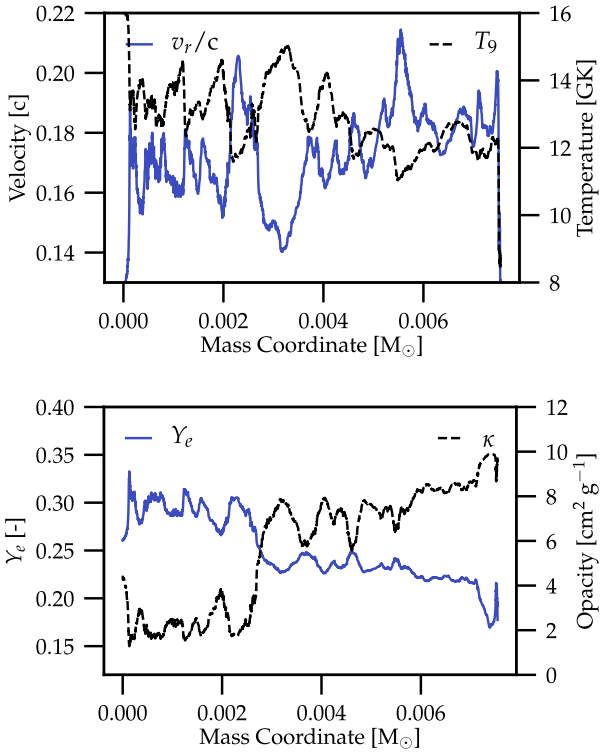

Figure 9. Averaged quantities for the HMNS ejecta, as a function of mass coordinate, used as input profiles for SNEC. The top panel shows the velocity (solid blue line) and temperature (dashed black line) of the outflow while the bottom panel shows the Y_e (solid blue line) and the corresponding opacity (dashed black line).

factors. The changing behaviour of ejecta velocity as a function of mass coordinate broadly aligns with the time evolution seen in these 3D renderings. In particular, there is a brief decrease in the ejecta velocity over time before the outflow resumes steady-state operation, which is reflected in the dip in the velocity profile around mass coordinate $\sim 3.0 \times 10^{-3}$ M$_\odot$. The electron fraction of the ejecta increases systematically as we move inward in mass coordinate. A negligibly small amount of material, located in the outermost layers, has $Y_e \lesssim 0.2$, while a substantial fraction of the ejecta with a total mass of $\sim 4.8 \times 10^{-3}$ M$_\odot$ has slightly higher values of $0.2 \lesssim Y_e \lesssim 0.25$. Finally, material below mass coordinate $\sim 2.7 \times 10^{-3}$ M$_\odot$ has intermediate values of $0.25 \lesssim Y_e \lesssim 0.35$. The corresponding opacities are ~ 10 cm^2 g^{-1} for the outermost, low-Y_e layers of the ejecta, between $\sim 5 - 10$ cm^2 g^{-1} for the bulk of the ejecta, declining as we move inward in mass coordinate to $\sim 1 - 5.5$ cm^2 g^{-1} for the inner ejecta with $Y_e \gtrsim 0.25$.

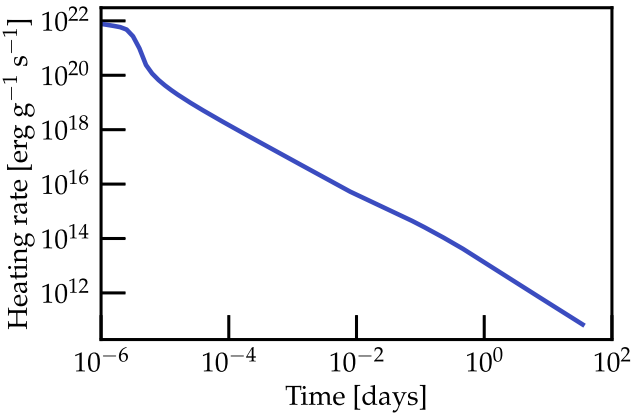

Figure 11. Radioactive heating rate per unit mass due to the decay of *r*-process material as a function of time as computed by KNEC.

The majority of the energy release due to radioactive decay of *r*-process nuclei happens on a timescale of $\sim$ seconds, as can also be seen in Fig. 11. However, most of the initial heat in the ejecta is lost through adiabatic expansion because the optical depth is very high and the thermal energy cannot yet escape as radiation. In Fig. 12, we show the evolution of the temperature of the outflow in SNEC, along with the photospheric radius and bolometric luminosity. The location of the photosphere is shown by the vertical dashed lines. From Fig. 12, we can see that the ejecta have cooled through expansion from initial temperatures of the order of $\sim 10^{10}$ K to temperatures around $\sim 10^5$ K within a couple of hours. As the ejecta expand and the density decreases, the photon diffusion time also decreases. The photosphere moves inward in mass coordinate (although still outward in radius) through the relatively high-opacity material in the outer layers. Significant electromagnetic emission becomes possible when the density is sufficiently low such that the photons can escape the ejecta on the timescale of expansion $\sim R/v$. This condition sets the characteristic radius at which the luminosity peaks and the corresponding time to peak. For these ejecta, the bolometric luminosity hits its peak at around one day, as expected for a low-mass, high-velocity outflow. The value of the peak luminosity depends sensitively on opacities and the amount of radioactive heating that occurs over the time to peak. The ejecta continue to expand and cool and the photosphere reaches the center

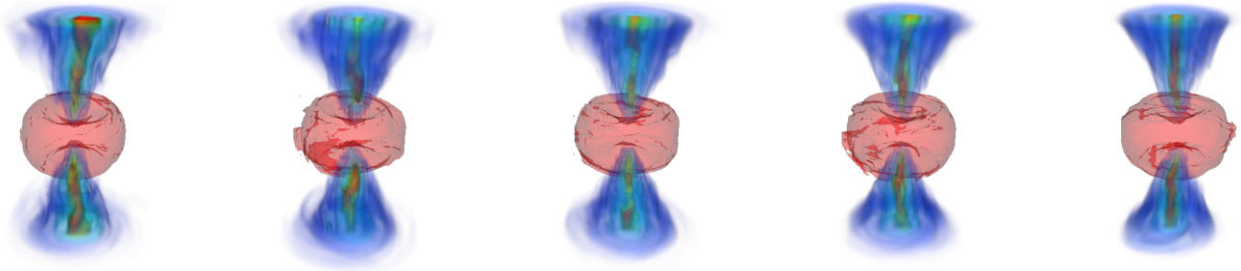

Figure 10. Volume renderings of the Bernoulli criterion (blue colormap) indicating unbound material and the disk contour at $\rho = 10^{10}$ g cm^{-3} (red) for model B15-low. The renderings (from left to right) depict the simulation at $t - t_{\rm map} = 9$, 12, 15, 18, and 21 ms. The z-axis is the rotation axis of the HMNS and we show the innermost 357 km. The colormap is chosen such that blue corresponds to material with lower Lorentz factors $-hu_t \simeq 1$, while yellow corresponds to material with $-hu_t \simeq 1.5$, and red to material with $-hu_t \simeq 2 - 5$. We note that for rendering purposes we have excluded part of the unbound ejecta in the equatorial region.

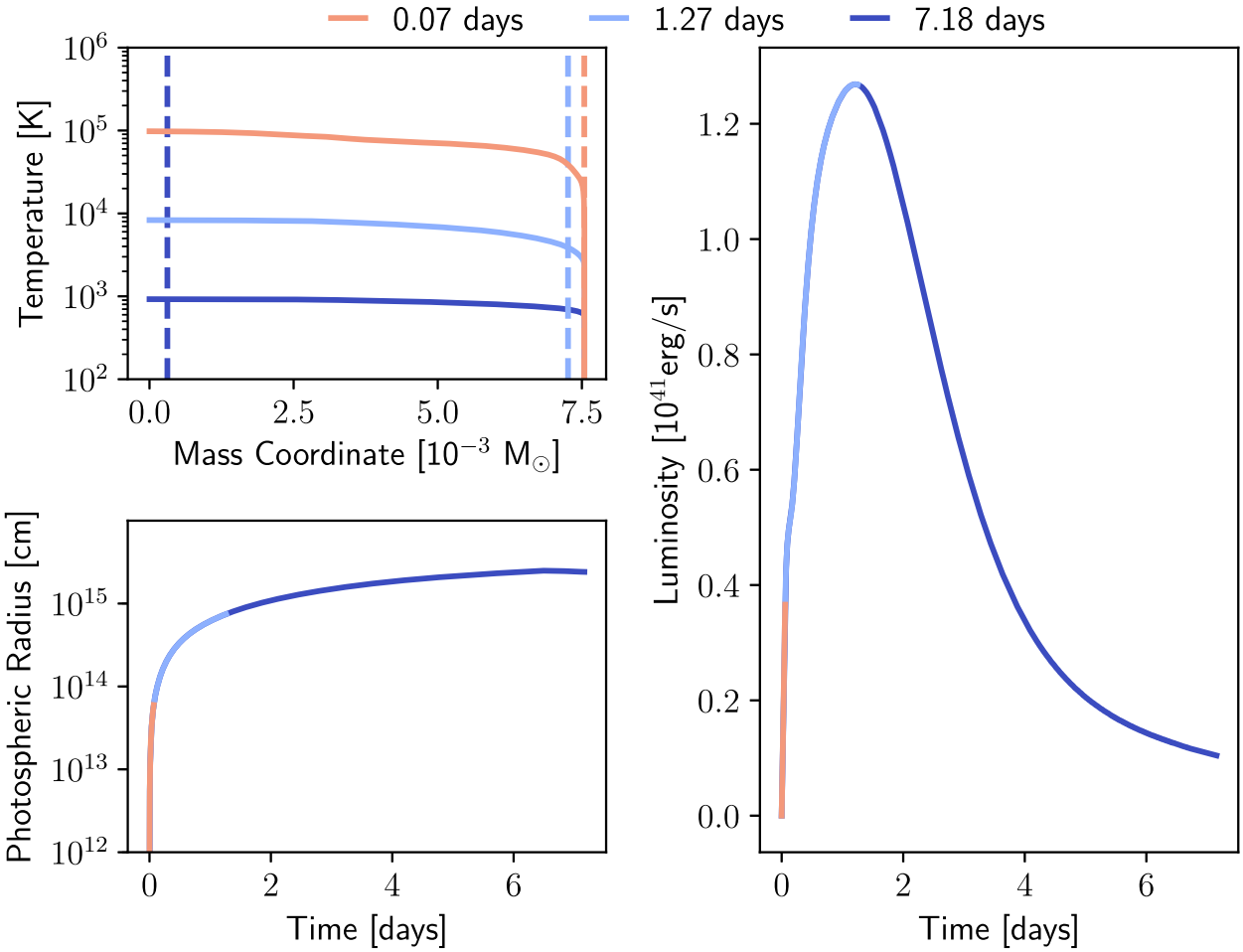

Figure 12. Evolution of the temperature profile of the outflow, the radius of the photosphere, and the bolometric luminosity of the kilonova as computed with SNEC. The three colours correspond to three different times: the peach line depicts the evolution up to a time of 0.07 days, the light blue line up to 1.27 days and the deep blue line up to 7.18 days. The vertical dashed lines in the top left panel represent the location of the photosphere in mass coordinate at these three times.

at $\sim$ 8.19 d when the entire ejecta become transparent to radiation. Beyond this point, the concept of a photosphere is no longer relevant and the observed luminosity is governed entirely by the radioactive heating rate.

The bolometric light curve of the kilonova is shown in Fig. 13, along with the luminosity at the photosphere. Given the velocity and opacity distribution of our ejecta, a simple spherical free-expansion model would suggest a peak timescale of $\sim$ 1–3 d. The peak luminosity, which depends on the amount of radioactive heating that occurs on the peak timescale, can be estimated to be of the order of $\sim 10^{41}$ erg s^{-1}. In keeping with these estimates, the bolometric light curve peaks at $L_{\rm obs}$ $\sim$1.27 $\times$ 10^{41} erg s^{-1} at roughly 1.2 d. The effective temperature at the photosphere is $\sim$4257 K at peak luminosity.

In Fig. 14, we present the corresponding AB magnitudes in optical (*ugriz*) and near-infrared (JHK$_s$) filters, produced under the assumption of blackbody emission at the photosphere and for the layers above the photosphere. The distance between the observer and the kilonova is taken to be 40 Mpc, same as the approximate distance to AT2017gfo. The black dotted line gives the evolution of the effective temperature computed at the photosphere. The shorter wavelength bands peak first since the effective temperature at the photosphere decreases as the ejecta expand and cool. By the time

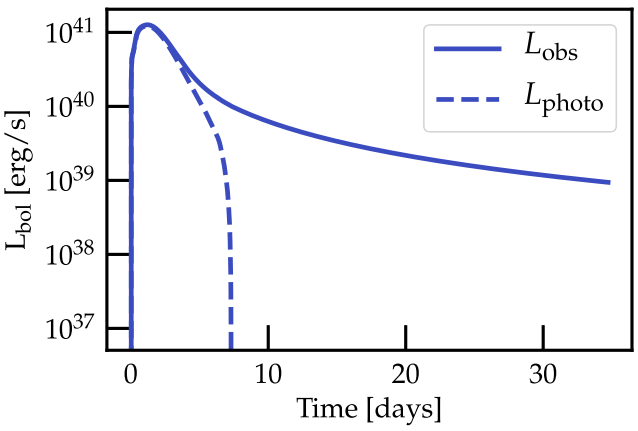

Figure 13. Observed bolometric luminosity (solid line) and the luminosity at the photosphere (dashed line) as a function of time.

the bolometric luminosity hits its peak, the effective temperature has dropped to $\sim$4257 K and continues to decrease rapidly, shifting the spectral energy distribution towards longer wavelengths and further into the infrared. The lowest peak magnitudes and hence

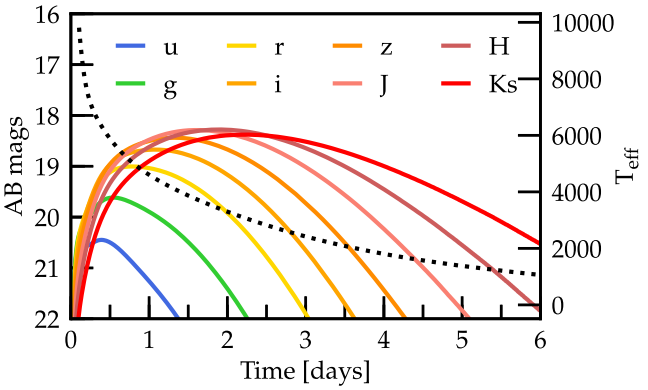

Figure 14. AB magnitudes of the kilonova in the *ugriz*JHK$_s$ bands are shown by solid colored lines. The dotted black line gives the evolution of the effective temperature at the photosphere. The distance between the observer and the kilonova is taken to be 40 Mpc, same as the approximate distance to AT2017gfo.

the brightest emission is seen in the J and H bands around day 2, both attaining a magnitude of ∼18.3 at 1.6 and 1.9 d, respectively. Although the fast evolution of the bolometric luminosity and a peak timescale of around a day are consistent with low-opacity high-Y_e outflows that produce a kilonova with a blue spectral peak, the band light curves for these ejecta peak in the infrared. This is due to the presence of high opacity material in the outer layers of the ejecta. By the time the ejecta expand enough to radiate efficiently, they have also cooled down substantially and the majority of the observed emission happens at longer wavelengths.

4 SUMMARY AND DISCUSSION

We have predicted *r*-process abundances and kilonova emission for outflows from HMNS remnants based on a dynamical 3D GRMHD simulation. The simulation includes a nuclear EOS and neutrino effects through a leakage scheme. To bracket possible uncertainties in the composition due to the approximate neutrino treatment, we have employed a range of constant neutrino luminosities during nucleosynthetic post-processing. We have mapped the outflow to an equilibrium-diffusion radiation hydrodynamics code to predict the bolometric light curve of the resulting kilonova as well as AB magnitudes in *ugriz*JHK$_s$ bands assuming blackbody emission. Our main findings are:

(i) The ejecta show a wide distribution in their Y_e, peaking in the ∼0.25–0.4 range depending on the choice of neutrino luminosity during post-processing. We do not find a robust third *r*-process peak and abundances beyond the second peak are reduced for constant luminosities above 10^{52} erg s^{-1}. This change in abundances aligns with the shifting peak of the Y_e distribution towards higher values.

(ii) The averaged spherically symmetric profiles of the ejecta shows outflow velocities between ∼ 0.15–0.2*c* and Y_e between ∼ 0.2–0.35, with a total ejecta mass of ∼7.5 × 10^{-3} M$_\odot$. The low Y_e, high-opacity ejecta lies ahead of the high Y_e, low-opacity ejecta in mass coordinate.

(iii) The bolometric light curve of the kilonova peaks at roughly one day with a luminosity of ∼ 10^{41} erg s^{-1} at peak, as expected for a low mass and high velocity outflow and given the heating supplied by decay of *r*-process nuclei.

(iv) The brightest emission is seen in the J and H infrared bands with a peak magnitude of ∼18.3, corresponding to effective photospheric temperatures of the order of ∼4000 K.

These HMNS ejecta represent a distinct and important part of BNS outflows in addition to the dynamical ejecta and accretion disk winds. For longer-lived remnants they could constitute the dominant component setting the *r*-process yields and kilonova properties. The bulk of the dynamical ejecta has much lower Y_e in comparison and a comparable total mass, while the disk winds have much lower velocities than HMNS ejecta. Both dynamical ejecta and disk winds are expected to make substantial amounts of lanthanides and produce a redder kilonova. For magnetically accelerated HMNS winds, however, the ejecta Y_e depends sensitively on the dynamics and it is possible for the Y_e in the outflow to be high enough to inhibit the synthesis of a substantial mass-fraction of lanthanides, and for the kilonova to consequently peak at visible wavelengths. This work is the first to predict the composition of HMNS ejecta and the nature of the resulting kilonova using realistic ejecta properties extracted from a 3D GRMHD dynamical simulation. Similar analysis of the dynamical ejecta from neutron star mergers has been carried out in Kullmann et al. (2022) and Just et al. (2022) based on GRHD simulations. Kawaguchi et al. (2021) have studied the long-term evolution of neutron star merger ejecta for the case where a long-lived neutron star remnant forms using outflow data from numerical relativity simulations that do not include magnetic fields.

Here, we have shown that HMNS outflows will not produce a robust third *r*-process peak and the lanthanide fraction in these ejecta depends on the neutrino luminosity encountered. The relatively high Y_e and lack of heavy *r*-process elements is in good agreement with previous axisymmetric viscous hydrodynamics studies presented in Fujibayashi et al. (2018) and Fujibayashi et al. (2020). Additionally, given the ejecta properties obtained here, the kilonova observed will peak around 1 d and in the infrared bands.

However, this picture may change for longer-lived remnants and if the evolution of the ejecta properties is followed over a longer time period. For longer remnant lifetimes, the total ejecta mass will be higher, resulting in a more luminous kilonova. We time-extrapolated the ejecta profiles assuming a HMNS lifetime of 100ms to obtain a larger total ejecta mass ∼ 10^{-2} M$_\odot$ and found that the resulting kilonova is more luminous but the behaviour across different wavelength bands remains mostly unchanged. The electron fraction distribution of the outflow will also shift to higher values over time. While the nucleosynthesis predictions presented in this work account for the effects of uncertain neutrino luminosities and the Y_e evolution of the tracer particles beyond the end of the hydrodynamical data, these aspects are currently not accounted for in the kilonova calculation. We directly use the outflow properties recorded at an extraction radius of r = 100 M$_\odot$ =148 km to predict the resulting kilonova emission. Especially for neutrino luminosities ∼10^{53} erg s^{-1}, it may be possible to remove the high opacity material or lanthanide curtain (Kasen, Fernández & Metzger 2015; Wollaeger et al. 2018; Nativi et al. 2021) in the outer layers of the ejecta, allowing the kilonova to peak in bluer bands. Additionally, we currently neglect the ejecta composition and compute band light curves assuming blackbody radiation at the effective temperature instead of using detailed opacities.

Further exploration of the kilonova counterpart will require tracking the outflow properties over a longer time period than we have considered here, taking into account the ejecta morphology as well as its composition, and employing de-

tailed wavelength-dependent opacities. The total mass, velocity, and electron–fraction distribution of these outflows broadly align with the derived values for the blue kilonova component associated with GW170817, indicating that detailed long-term end-to-end modeling is needed to definitively answer the question of whether HMNS ejecta can produce a blue kilonova.

ACKNOWLEDGEMENTS

DR acknowledges funding from the U.S. Department of Energy, Office of Science, Division of Nuclear Physics under Award Number(s) DE-SC0021177 and from the National Science Foundation under Grants No. PHY-2011725, PHY-2020275, PHY-2116686, and AST-2108467.

DATA AVAILABILITY

The data underlying this article will be shared on reasonable request to the corresponding author.

REFERENCES

Abbott B. P. et al., 2017, ApJ, 848, L12
Arcavi I. et al., 2017, Nature, 551, 64
Chornock R. et al., 2017, ApJ, 848, L19
Coulter D. A. et al., 2017, Science, 358, 1556
Cowan J. J., Sneden C., Lawler J. E., Aprahamian A., Wiescher M., Langanke K., Martínez-Pinedo G., Thielemann F.-K., 2021, Rev. Mod. Phys., 93, 015002
Cowperthwaite P. S. et al., 2017, ApJ, 848, L17
Cyburt R. H. et al., 2010, ApJS, 189, 240
Drout M. R. et al., 2017, Science, 358, 1570
Evans P. A. et al., 2017, Science, 358, 1565
Fahlman S., Fernández R., 2018, ApJ, 869, L3
Frankel S., Metropolis N., 1947, Phys. Rev., 72, 914
Fujibayashi S., Kiuchi K., Nishimura N., Sekiguchi Y., Shibata M., 2018, ApJ, 860, 64
Fujibayashi S., Wanajo S., Kiuchi K., Kyutoku K., Sekiguchi Y., Shibata M., 2020, ApJ, 901, 122
Fuller G. M., Fowler W. A., Newman M. J., 1982, ApJS, 48, 279
Goriely S., Bauswein A., Janka H.-T., 2011, ApJ, 738, L32
Just O., Kullmann I., Goriely S., Bauswein A., Janka H. T., Collins C. E., 2022, MNRAS, 510, 2820
Kasen D., Badnell N. R., Barnes J., 2013, ApJ, 774, 25
Kasen D., Fernández R., Metzger B. D., 2015, MNRAS, 450, 1777
Kasen D., Metzger B., Barnes J., Quataert E., Ramirez-Ruiz E., 2017, Nature, 551, 80
Kawaguchi K., Fujibayashi S., Shibata M., Tanaka M., Wanajo S., 2021, ApJ, 913, 100
Korobkin O., Rosswog S., Arcones A., Winteler C., 2012, MNRAS, 426, 1940
Kullmann I., Goriely S., Just O., Ardevol-Pulpillo R., Bauswein A., Janka H. T., 2022, MNRAS, 510, 2804
Langanke K., Martínez-Pinedo G., 2000, Nucl. Phys. A, 673, 481
Lattimer J. M., Swesty D. F., 1991, Nucl. Phys. A, 535, 331
Lattimer J. M., Mackie F., Ravenhall D. G., Schramm D. N., 1977, ApJ, 213, 225
Li L.-X., Paczyński B., 1998, ApJ, 507, L59
Lippuner J., Roberts L. F., 2017, ApJS, 233, 18
Mamdouh A., Pearson J. M., Rayet M., Tondeur F., 2001, Nucl. Phys. A, 679, 337
McCully C. et al., 2017, ApJ, 848, L32
Metzger B. D. et al., 2010, MNRAS, 406, 2650
Metzger B. D., Thompson T. A., Quataert E., 2018, ApJ, 856, 101
Meyer B. S., 1989, ApJ, 343, 254
Morozova V., Piro A. L., Renzo M., Ott C. D., Clausen D., Couch S. M., Ellis J., Roberts L. F., 2015, ApJ, 814, 63
Mösta P., Radice D., Haas R., Schnetter E., Bernuzzi S., 2020, ApJ, 901, L37
Nativi L., Bulla M., Rosswog S., Lundman C., Kowal G., Gizzi D., Lamb G. P., Perego A., 2021, MNRAS, 500, 1772
Nedora V., Bernuzzi S., Radice D., Perego A., Endrizzi A., Ortiz N., 2019, ApJ, 886, L30
Nicholl M. et al., 2017, ApJ, 848, L18
O'Connor E., Ott C. D., 2010, Class. Quantum Gravity, 27, 114103
Oda T., Hino M., Muto K., Takahara M., Sato K., 1994, At. Data Nucl. Data Tables, 56, 231
Ott C. D. et al., 2013, ApJ, 768, 115
Panov I. V., Ptitsyn D. A., Chechetkin V. M., 1995, Astron. Lett., 21, 185
Perego A. et al., 2022, ApJ, 925, 22
Pian E. et al., 2017, Nature, 551, 67
Qian Y. Z., Woosley S. E., 1996, ApJ, 471, 331
Radice D., Perego A., Hotokezaka K., Fromm S. A., Bernuzzi S., Roberts L. F., 2018, ApJ, 869, 130
Roberts L. F., Kasen D., Lee W. H., Ramirez-Ruiz E., 2011, ApJ, 736, L21
Soares-Santos M. et al., 2017, ApJ, 848, L16
Symbalisty E., Schramm D. N., 1982, Astrophys. Lett., 22, 143
Tanaka M. et al., 2018, ApJ, 852, 109
Tanvir N. R. et al., 2017, ApJ, 848, L27
Villar V. A. et al., 2017, ApJ, 851, L21
Wollaeger R. T. et al., 2018, MNRAS, 478, 3298
Wu Z., Ricigliano G., Kashyap R., Perego A., Radice D., 2022, MNRAS, 512, 328

This paper has been typeset from a TEX/LATEX file prepared by the author.